Deliniating the deep crustal fluid link between the Paralana Enhanced Geothermal System and the Beverley Uranium Mine using Magnetotellurics

Thesis submitted in accordance with the requirements of the University of Adelaide for an Honours Degree in Geophysics.

Paul Soeffky

November 29, 2012

THE UNIVERSITY of ADELAIDE

ABSTRACT

The global demand for clean energy alternatives is constantly increasing, creating significant interest for more sustainable energy resources such as uranium and geothermal. Australia is host to over 25% of the world's known uranium resources as well as having significant geothermal potential.

The Mount Painter Domain, in the Northern Flinders Ranges in South Australia, is in a region of anomalously high heat flow generated by radiogenic decay of uranium and thorium rich granites. Two distinct uranium deposits have formed from dissolved uranium carried from the ranges by fluids, being deposited where reduction in sediment pH precipitates uranium.

In May 2012 a magnetotelluric profile was collected, extending from the Northern Flinders Ranges to the Lake Frome embayment to help constrain existing resistivity models. Precipitation of uranium at the Beverley Mine site is anomalous as no surface water flow is present, suggesting the presence of subsurface processes. This pathway is linked to a $50\,\Omega\,\mathrm{m}$ conductive body at the brittle-ductile boundary of the mid-crust, directly under the Paralana geothermal prospect. 3D modelling of the Paralana geothermal prospect suggest deep conductive features connecting with features at the surface.

KEYWORDS

magnetotellurics, uranium exploration, fluids, three-dimensional inversion, geothermal, electromagnetic induction, graphite

Table of Contents

List of Figures

INTRODUCTION

The north-eastern Flinders Ranges host uranium rich granites which have a two-fold effect on the local geological environment. Heat production due to radiogenic decay of the basement rock has resulted in the presence of a significant geothermal potential at Paralana, while the erosion of the ranges has resulted in the formation of uranium deposits at their base. Understanding the uranium depositional pathways is important in exploring for future targets, while defining the Paralana geothermal system enables efficient production of renewable energy. This study proposes to gain a better appreciation for processes surrounding both of these resources and the relationship between the two areas.

Paralana is located on the east facing plains of the north-eastern Flinders Ranges, within the South Australian Heat Flow Anomaly (SAHFA) as defined by Neumann et al. (2000). Anomalous heat flow measurements of up to $126\,\mathrm{mW/m^2}$ have been recorded close to Paralana in the Mount Painter Domain (MPD) (Neumann et al. 2000; Brugger et al. 2005). The regional geothermal gradient for Paralana is $50 - 70°\mathrm{C\ km^{-1}}$ (Cull & Conley 1983), significantly higher than the global average value for intraplate sites (Fridleifsson et al. 2008). The north-eastern Flinders Ranges around the Paralana area consist of exposed radiogenic granite belonging to the MPD. The Paralana plains are comprised of sediments derived from erosion of the adjacent MPD granites, thickening eastwards towards Lake Frome. These sediments act as an insulating thermal blanket over the heat producing granites (Heathgate Resources 1998; Neumann et al. 2000; Huenges & Ledru 2010; PIRSA 2011).

The uranium rich granitic basement rocks of Paralana are present in the Flinders Ranges, where the MPD has been uplifted. These have been eroded, transporting uranium to be deposited in palaeochannels on the plains below (Heathgate Resources 1998;

Märten 2006). Reductive fluids play an important part in uranium deposition, as uranium is most mobile as an oxide. It has been suggested that the Beverley and Four Mile Creek uranium deposits could be related to faults containing mobile reducing fluids, leading to the reduction and deposition of uranium out of the transporting water. The deposits contain over 1600 ppm of uranium at depth of 100-120 m within the sedimentary strata (Heathgate Resources 1998).

The Paralana geothermal system is an Enhanced Geothermal System (EGS); it contains very little fluid and requires additional fluid to be pumped into the hot rocks for it to become viable for energy production. The geothermal prospect is located at depths in excess of 3 km making it difficult to gather reliable geological information. The presence of high temperature rock in the subsurface and the existence of reductive fluids have altering effects on the local electrical resistivity, resulting in contrasting resistivity characteristics across the geothermal system boundaries which magnetotellurics (MT) can detect (Simpson & Bahr 2005; Aizawa et al. 2011; Peacock et al. 2012). The wide range in depth and resolutions offered by MT prescribes it as the preferred geophysical technique for locating and characterising geothermal prospects (Garg et al. 2007; Newman et al. 2008; Heise et al. 2008; Spichak & Manzella 2009; Peacock et al. 2012).

Although the individual uranium deposits at Beverley and Four Mile Creek are too small to be directly detected using MT, graphite mineralisation can be used as a deposit identifier. Graphite is a low resistivity mineral commonly associated with uranium deposits. Faults containing graphite enable uranium deposition through reduction, reducing uranium ions from soluble U^{6+} to insoluble U^{4+} ions (Tuncer 2007). Graphite has a significantly lower resistivity than non-metalliferous rock which enables it to be used as a marker for the uranium deposits when undertaking an MT survey (Duba &

Shankland 1982; Simpson & Bahr 2005; Farquharson & Craven 2009). Using MT, the conductive signature of the graphite, and ultimately the uranium can be mapped.

In this study, an MT survey has been collected over the Paralana EGS, encompassing the Beverley and Four Mile Creek uranium deposits to collect resistivity information. Broadband MT sensors were used for near surface resolution, while long period sensors were used to give resolution to a much greater depth. The 3D structure of the Paralana EGS has been explored by creating a 3D inversion model using the data collected, in conjunction with existing MT data from Peacock et al. (2012) and Thiel et al. (2012). Additionally, a 2D inversion model has been created over the survey line, providing evidence as to how the Beverley and Four Mile Creek uranium deposits are related to the Paralana EGS.

BACKGROUND

The area of focus for this investigation is located in the north-eastern Flinders Ranges, in South Australia (Figure 1). The study area extends from the Flinders Ranges in the west to the edge of Lake Frome in the east. The MPD makes up the lithology of the western side of the study area and the eastern region consists of the Lake Frome embayment (Figure 2). All this sits stratigraphically above the Curnamona Province consisting of sediments, volcanics and granites of Palaeoproterozoic to Mesoproterozoic age (Neumann et al. 2000; PIRSA 2011).

The MPD consists of Mesoproterozoic granites, gneisses and meta-sediments that have been overlain by Neoproterozoic to Cambrian sediments belonging to the Adelaide Geosyncline (Coats & Blissett 1971; Preiss & Forbes 1981; Preiss 1990; Neumann

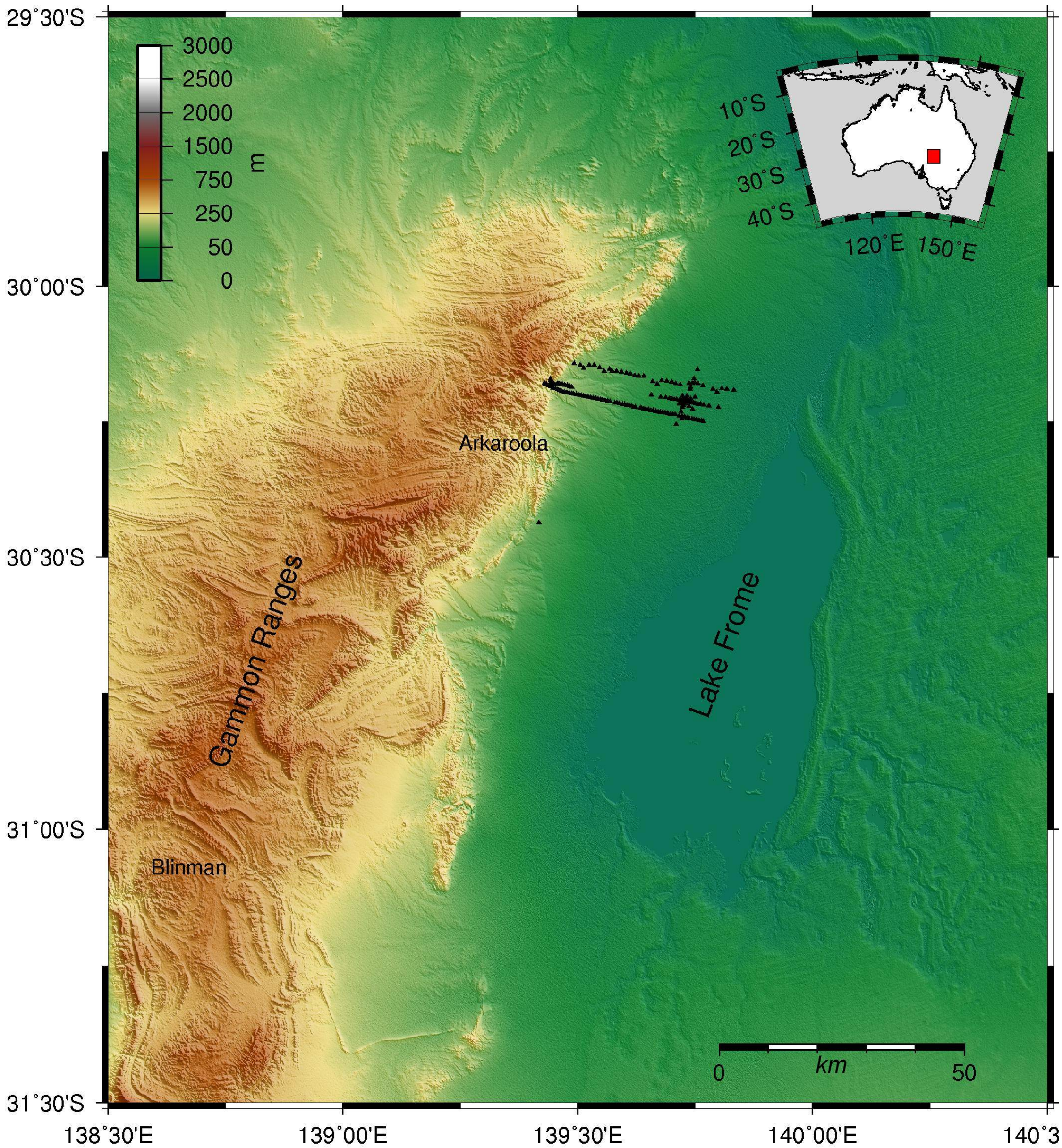

Figure 1: A regional topographic map containing the two parallel survey lines. Individual station locations are marked by black triangles, with the north and south lines clearly visible. A third survey designed for 3D modelling can be seen forming a cross of stations, centred around the Paralana borehole.

et al. 2000). The Paralana fault system forms the eastern boundary of the MPD and causes it to be thrust over the sediments of the Lake Frome embayment (Coats & Blissett 1971). The Lake Frome embayment lies at the southern margin of the Great Artesian

Basin (Cox & Barron 1998). The Great Artesian Basin sediments range in age from Late Triassic to Late Cretaceous and have been overlain in the Lake Frome Embayment by Tertiary fluvio-lacustrine sediments capped by silcrete and duricrust resulting from deep chemical weathering (Brugger et al. 2005).

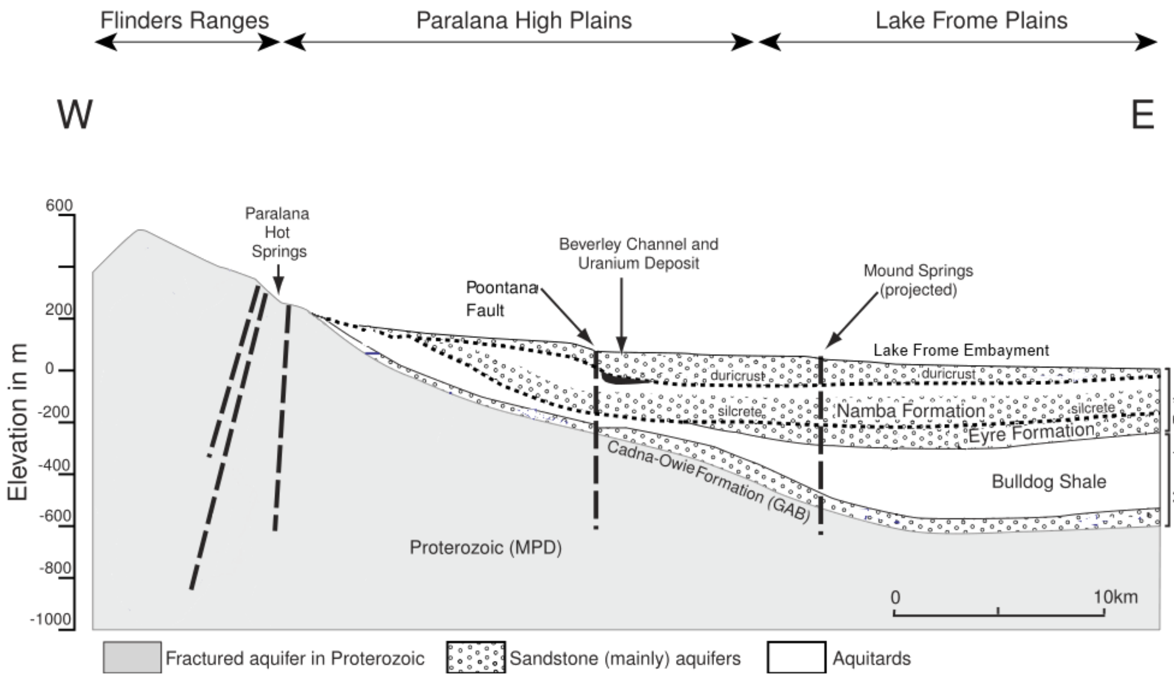

Figure 2: A cross section of the stratigraphy from the Mt. Painter Domain to the Lake Frome Embayment, showing the different ages of the rock units and their stratigraphic relationship. Faults are marked by black dashed lines and are projected through the subsurface. The Beverly Uranium deposit is located in a palaeochannel with the Poontana fault defining the western edge. Modified from Heathgate Resources (1998)

The surface heat flow in the MPD has been recorded to be as high as 126 mW/m^2 (Neumann et al. 2000), significantly higher than the radiogenic component of the global heat flow average of 20 - 44 mW/m^2 (Pinet & Jaupart 1987; Ketcham 1996; McLennan & Taylor 1996; Rudnick et al. 1998). The MPD lies inside a region of anomalously high heat flow defined by Neumann et al. (2000) as the SAHFA. The SAHFA is centred on the western margin of the Adelaide Geosyncline and extends to encompass the eastern half of the Gawler Craton and the Stuart Shelf in the west and the Curnamona province in the east, where the regional average surface heat flow can be confined to a range of 82-102 mW/m^2 (Cull 1982; Sandiford et al. 1998; Neumann et al. 2000; Brugger et al. 2005).

The Paralana geothermal prospect is located in the middle of the SAHFA. Petratherm have drilled a 4 km borehole in the centre of the prospect (Petratherm 2012). The high heat flow is unusual as the heat source is not magmatic, but due to radiogenic decay of radioactive elements such as uranium and thorium, contained within the granitic basement (Sandiford et al. 1998; Neumann et al. 2000; Brugger et al. 2005). The high geothermal gradient, mentioned in the Introduction, is linked to both the geothermal potential at Paralana and the Paralana Hot Springs, located further to the west in the Flinders Ranges. The meteoric water source for these springs is heated to temperatures between 56°C and 63°C by the same radiogenic heat source as the geothermal prospect but at a much shallower depth (Brugger et al. 2005).

The granitic basement rocks generating high amounts of heat for the Paralana geothermal system have another significant effect on the area. The MPD has been uplifted to form the north eastern tip of the Flinders Ranges. The first uranium deposits in the region were discovered in 1969 (Heathgate Resources 1998) and have been found to be secondary deposits deposited within palaeochannels of the Tertiary age sediments of the Lake Frome Embayment (Heathgate Resources 1998; Märten 2006). The uranium bearing palaeochannel sands are bounded by clays above and below and the impermeable Poontana Fault Zone to the west (Figure 2). The ore bodies are at a depth of 100-120 m and have a thickness of about 10 m (Heathgate Resources 1998; Brugger et al. 2005; Märten 2006). It has been suggested that the uranium deposits around Beverley and Four Mile Creek could be fault controlled, where the uranium containing water mixed with mobile reductants in a fault zone, causing deposition of the uranium

(Skirrow et al. 2009).

Magnetotelluric Theory

The passive electromagnetic technique, MT, records fluctuations in the Earth's electric (**E**) and magnetic (**B**) fields (Simpson & Bahr 2005). Surface measurements are recorded in orthogonal directions, generally orientated parallel (x), perpendicular (y) with respect to geoelectric strike, and vertical (z), also know as the Tipper. Induced electric and magnetic fields are perpendicular to the inducing fields and can be separated into two modes. The transverse electric (TE) mode contains the electric field (E_x) parallel to strike and the associated magnetic field (B_y) is perpendicular to strike. The TE mode records current flow parallel to strike. The transverse magnetic (TM) mode contains the magnetic field (B_x) parallel to strike and the electric field (E_y) perpendicular to strike. The TM mode records current flow perpendicular to strike (Simpson & Bahr 2005). The relationship between the horizontal components of the electric and magnetic fields is defined by the impedance tensor (Z):

$$\mathbf{E} = \mathrm{Z}\mathbf{B}/\mu_0 \qquad \text{or} \qquad \begin{pmatrix} E_x \\ E_y \end{pmatrix} = \begin{pmatrix} Z_{xx} & Z_{xy} \\ Z_{yx} & Z_{yy} \end{pmatrix} \begin{pmatrix} B_x/\mu_0 \\ B_y/\mu_0 \end{pmatrix} \tag{1}$$

where μ_0 is the magnetic permeability, usually given as ($\mu_0 = 4\pi \times 10^{-7}\,\mathrm{H\,m^{-1}}$). The impedance tensor is used to determine the direction of geoelectric strike, the direction of dominant current flow. The impedance tensor is defined as:

$$\mathrm{Z} = \begin{pmatrix} 0 & Z_{xy} \\ Z_{yx} & 0 \end{pmatrix} \tag{2}$$

where the off diagonals are set to zero, indicating two dimensional (2D) current flow. The resolution and depth sensitivity can be manipulated by varying the recorded frequency, where higher frequencies result in greater resolution but less depth penetration. These properties are related using the electromagnetic skin depth equation:

$$p(T) = 500\sqrt{T\rho_a} \tag{3}$$

where $p(T)$ is the electromagnetic skin depth in metres at a given period (T) and ρ_a is the apparent resistivity at the period (T) (Simpson & Bahr 2005).

MAGNETOTELLURIC DATA

Methodology

An MT survey was conducted along a 42 km east-west transect across Paralana and Beverley in the northern Flinders Ranges. The survey consisted of 35 broadband stations at 1 km intervals and 15 long-period sites, 3 km apart (Figure 3). The first station started recording on day 120 at 0300 UTC, 2012, and the final station stopped recording on day 128 at 0300 UTC, 2012. Broadband stations were set out recording 4-components (Bx, By, Ex, Ey) using AuScope instruments, while Bartington's fluxgate instruments were used at the long-period sites to record 5-components (Bx, By, Bz, Ex, Ey).

The recording instruments were time synchronised using GPS, to enable more reliable data correlation and remote referencing. Dipoles for all sites were approximately 50 m in length and consisted of non-polarising porous $Cu-CuSO_4$ pot electrodes orientated towards geographic North and East, magnetic induction coils were orientated parallel to the electrode dipoles. Broadband stations sampled at 500 Hz and recorded for two days

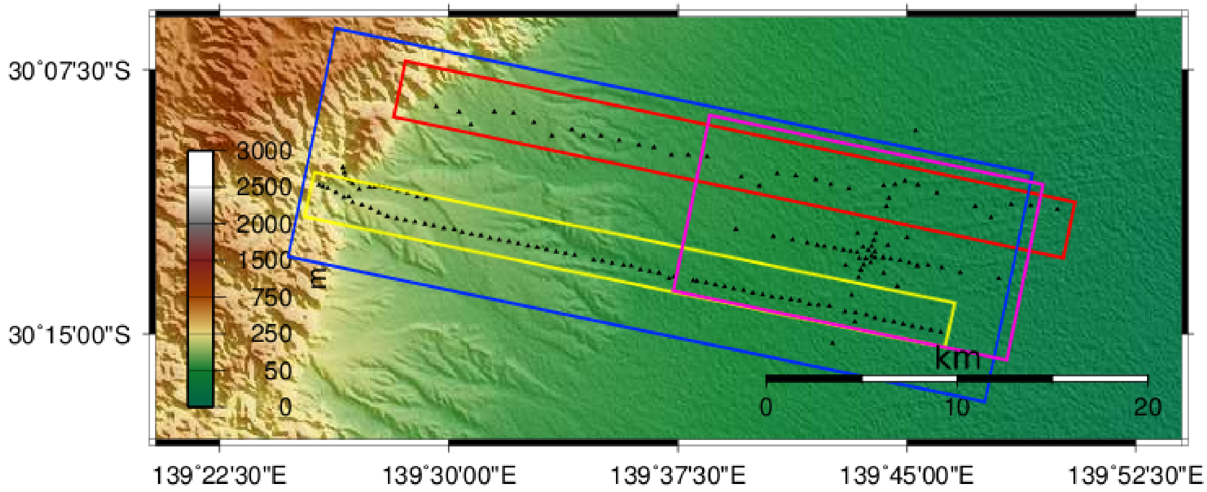

Figure 3: A close up topographic map of the station locations. The model boundaries are distinguished by different colour boxes. Northern 2D inversion in red, southern 2D inversion in yellow, broad scale 3D model in blue and 3D dense grid model in pink.

before being moved to a new location. Long-period stations recorded for three days, sampling at 10 Hz, before being moved to a new station location.

A site 60 km south-west of the survey line was chosen as the location for the broadband remote referencing station, which operated continuously throughout the survey. The long period stations were remote referenced using magnetic observatory data collected in Alice Springs. Both of the remote reference locations were time synchronised with the survey stations using the on board GPS.

Fluctuations in the electrical field strength (E) were calculated using the distance between dipoles (d) and the potential difference (V):

$$V = \mathrm{E} \cdot d \tag{4}$$

The raw broadband data were decimated, to obtain 50 Hz data. The three data sets (500, 50 and 10 Hz) were then combined using transfer functions into 5, 24, 48 and

72 (long period only) hour blocks using a robust bounded influence remote referencing method: BIRRP (Bounded Influence, Remote Reference Processing) (Chave & Thomson 2004). Remote referencing improved the signal to noise ratio, particularly in the dead band (0.5 - 5 Hz), where there is a noticeably lower signal strength (Figure 4)(Chave & Thomson 1989; Chave & Thomson 2004). The quality of the data was assessed based on apparent resistivity, phase and coherence plots produced by BIRRP, with noisy station data windows discarded and a new time window processed.

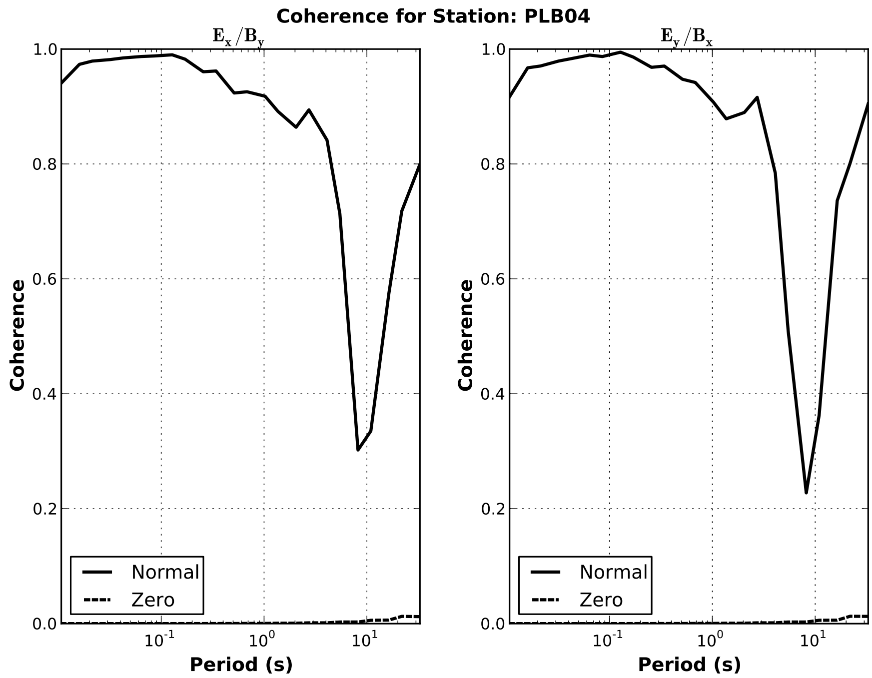

Figure 4: A coherence plot of station PLB04, demonstrating good coherence (> 0.8) between electric and magnetic response across all frequencies except in the dead band (0.5 - 5 Hz).

To model the data, the Occam inversion code developed by Constable et al. (1987) and outlined in deGroot Hedlin & Constable (1990), was used to produce a 2D inversion model from the EDI files. Error bars and smoothing parameters were used to control the model by adjusting the data fit tolerance of cells near the data points to achieve a geologically feasible model.

Three-dimensional (3D) modelling of the region was conducted using the data-space Occam inversion algorithm, WSINV3DMT (Siripunvaraporn et al. 2005; Siripunvaraporn & Egbert 2009; Siripunvaraporn 2012). Two models were generated due to computing power restrictions and the limitations of the algorithm. The data fit of the model was controlled by error bars and smoothing parameters in much the same was as the 2D model. A smooth model with poor data fit was first generated and used as the starting conditions for a second model with smaller error bars and greater data fit.

Induction Arrows

Induction arrows were generated from the long period data only, as the vertical magnetic field component (Bz) or Tipper, was not measured with broadband instruments. Induction arrows are used to determine the presence of lateral variations in conductivity which generate vertical magnetic fields (Simpson & Bahr 2005). The ratio of vertical to horizontal magnetic field components are represented by vector arrows, with the real component of the induction arrows plotted using the Parkinson convention, where the vectors point towards regions of high conductivity (Figure 5). The regional trend, established by the induction arrows, around Paralana is towards the north west. The small size of the inducting arrows indicates that this trend is weak and the conductivity gradient is shallow. The conductivity gradient decreases with depth, as the induction arrows decrease in size as the frequency becomes longer (Figure 5). The orientation of the arrows swings towards the east with depth, suggesting the regional conductive gradient is dipping towards the east.

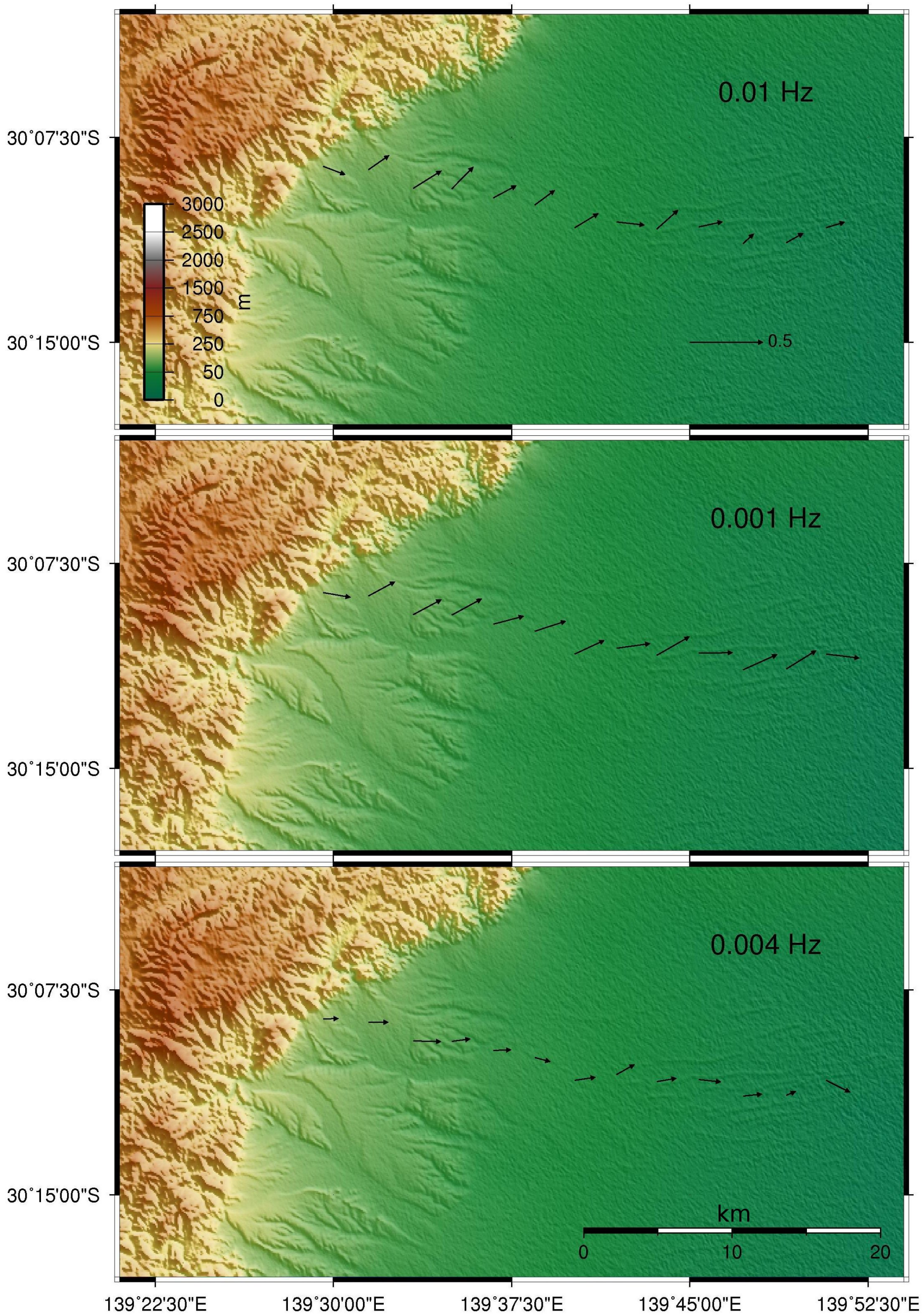

Figure 5: The real part of induction arrows from the long period MT sites collected across the northern line. The induction arrows are in the Parkinson convention and show a regional trend towards the north east. The length of the arrows is affected by the strength of the conductivity gradient and the distance from the site. Moving from top to bottom over the image, the frequency reduces (0.01 - 0.004 Hz) increasing the range of the induction arrows.

Phase Tensors

The MT phase tensor is a graphical representation of the invariant proportion of the impedance tensor, which is unaffected by small scale local structure (Figure 6) (Caldwell et al. 2004; Booker 2012). The principal components of the phase tensor indicate the horizontal directions of maximum and minimum induction current through the use of an ellipsoid (Caldwell et al. 2004). The maximum induction direction is represented by the maximum axis of the ellipsoid, supported by the induction arrows, and is orientated in the direction of highest conductivity. The size and shape of the phase tensor ellipses are indicative of the strength of induction. The phase angles $\Phi_{\max}$ and ($\Phi_{\min}$) are a measure of ellipticity (λ):

$$\lambda = \frac{|\Phi_{\max} - \Phi_{\min}|}{\Phi_{\max} + \Phi_{\min}} \tag{5}$$

where a low minimum phase angle represents high ellipticity and equal $\Phi_{\max}$ and $\Phi_{\min}$ values result in a cirle, indicating one dimensionality. The skew (β) of the phase tensor is a measure of 3D symmetry, asymmetric tensors have a skew angle greater than 0° (Bibby et al. 2005). The skew angle is the difference between the geoelectric strike and the direction of maximum conductivity. Circular tensors indicate near 1D structure, while elongate tensors are indicative of a strong induction polarisation. The lack of ellipticity in the phase tensors at high frequency is consistent with the presence of thick sediment cover over the plains, indicating the data is one dimensional (1D) (Figure 7). Comparing the phase tensor results at 1 Hz and 10 Hz, the sediments are thickening away from the Flinders Ranges (Figure 8). The majority of the phase tensors at 10 Hz are 1D, but at 1 Hz only the phase tensor further from the ranges are still 1D.

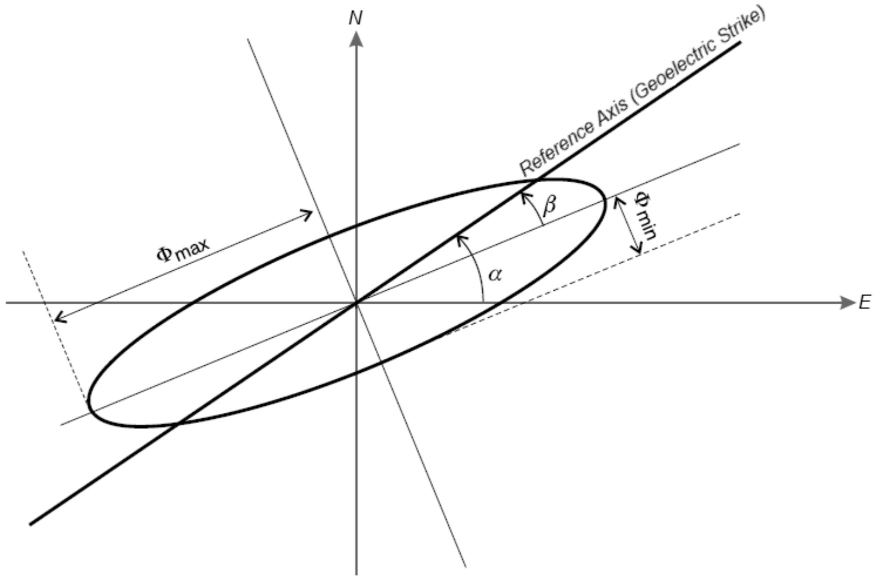

Figure 6: The phase tensor represented graphically as an ellipse. The axes of the ellipse are represented by the maximum and minimum phase (Φ_{max} and Φ_{min}), with the rotation away from the reference axis represented by the skew (β) and is a measure of 3D symmetry. The axes of the reference frame are arbitrarily orientated North and East and are independent of the tensor ellipse. Modified from Bibby et al. (2005)

Data gathered in the sediments does not contain 2D or 3D effects, but the underlying basement rock is suggested to be multidimensional. Phase tensor data collected along the northern survey line is consistent with previous data collected by Peacock et al. (2012), as the ellipses are similar in orientation and ellipticity. The basement rock that makes up the Flinders Ranges is highly resistive, demonstrated by the low minimum phase. Minimum phase decreases from west to east suggesting the depth to basement rock is increasing toward the east (Figure 8).

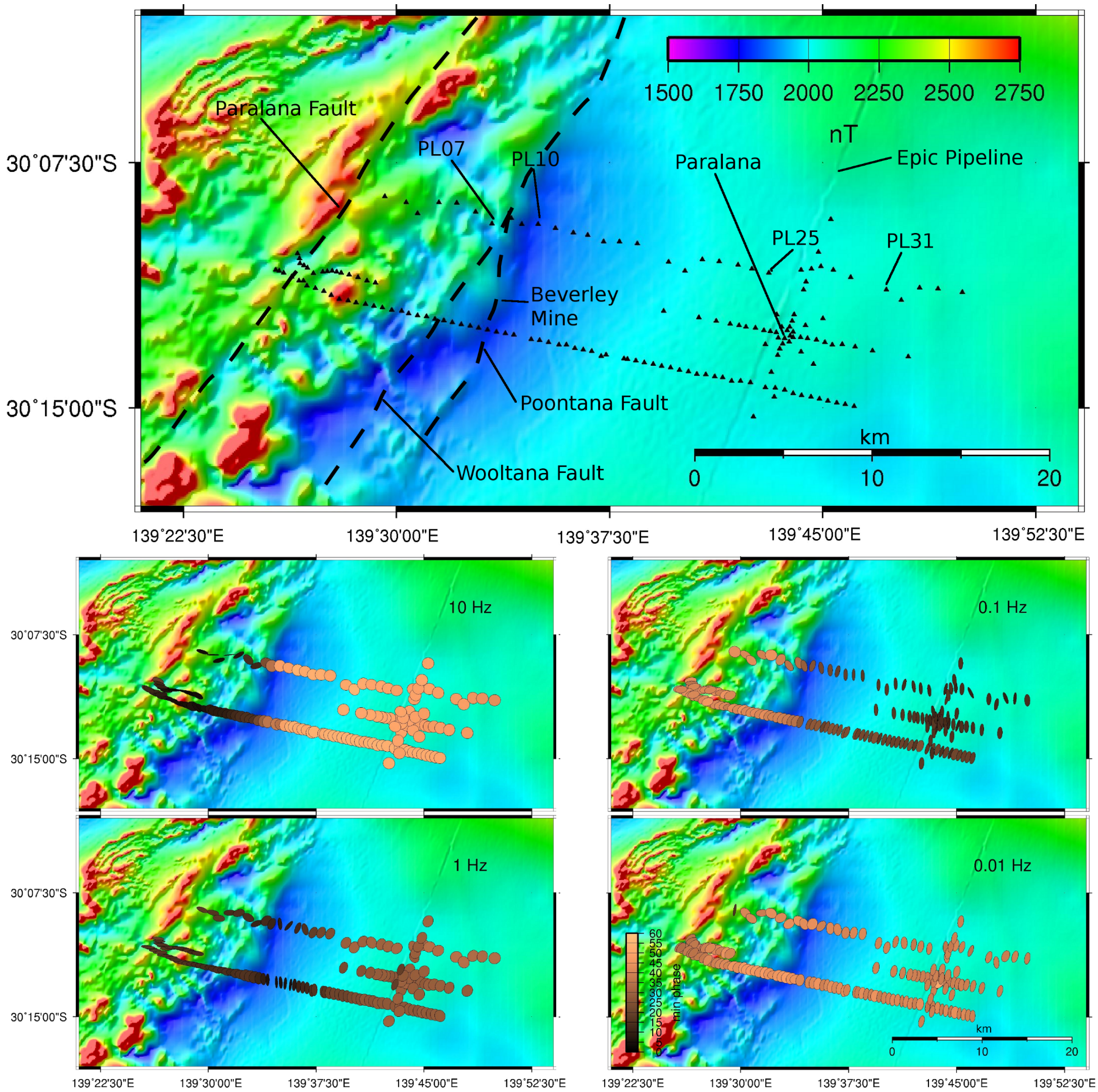

Figure 7: Phase tensors plotted on a total magnetic intensity (TMI) image. The TMI image at the top represents the survey area, with significant features annotated. The phase tensor ellipse represents the phase of the impedance tensor, where the major axis indicates the direction of current flow and the ellipticity is a measure of the adherence to the current flow direction. The colour is a representation of the invariant minimum phase value relating to conductivity changes with depth (small phase [black] relates to a low conductivity). Phase tensors are sensitive to crustal structure, with the four images decreasing in frequency from 10 Hz to 0.01 Hz, from upper left to lower right, to demonstrate variations in crustal structure with increasing depth.

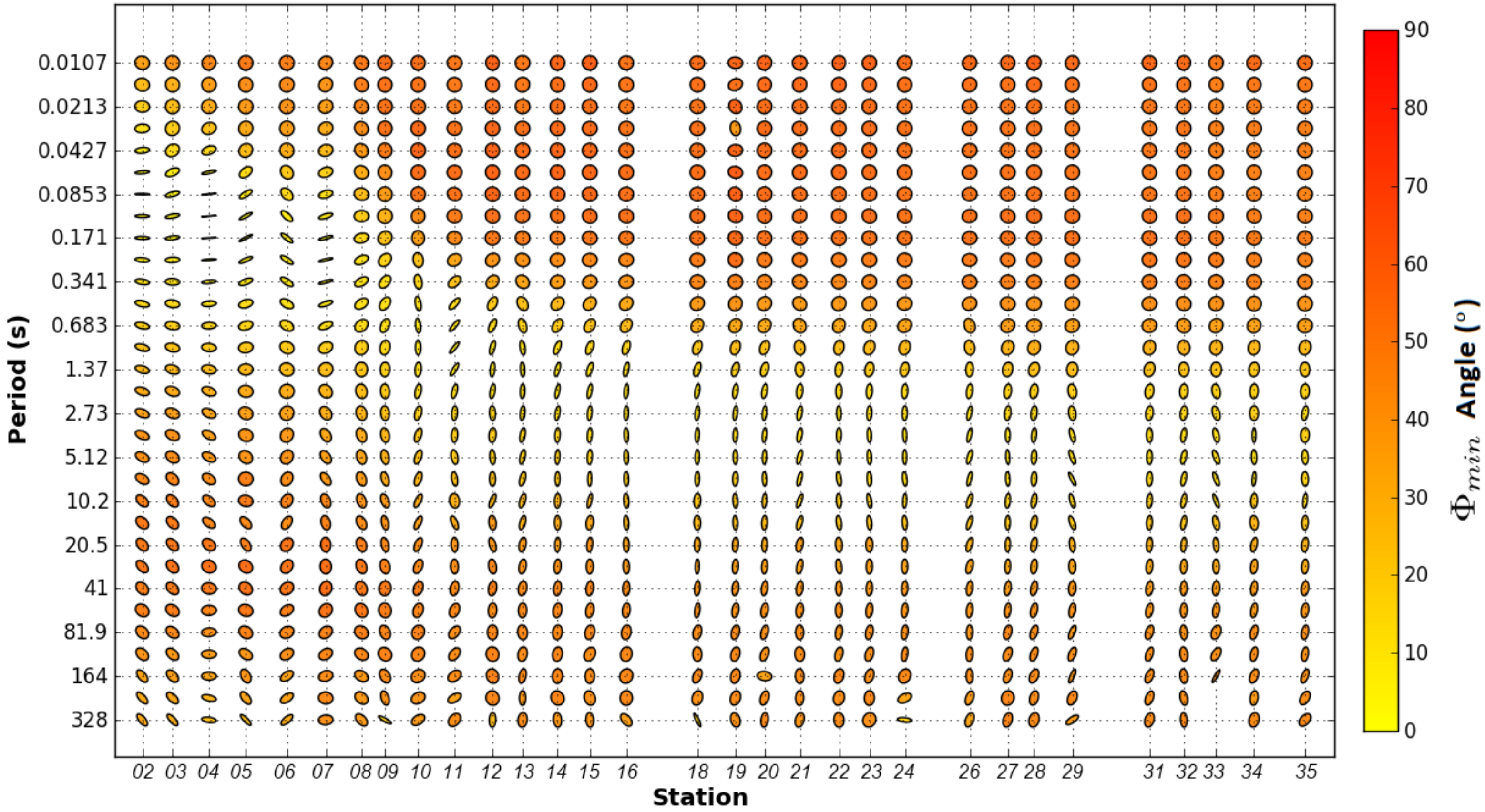

Figure 8: A 2D pseudo section of phase tensors across the northern line. Period on the y-axis is indicative of depth, with longer periods corresponding to greater depth. The basement rock can be observed to be dipping towards the east, as a region of high ellipticity and low minimum phase angle. Sediments lie above the basement rock and are represented by a region of high minimum phase angle and circular phase tensors.

Data Quality

INITIAL PROCESSING

The Epic gas pipeline, which was a significant source of noise affecting data quality during acquisition, is clearly visible on the TMI image, as a strong linear feature through the sediments. The noise generated by the pipeline had significant detrimental affects on the quality of data collected from the stations in close proximity. The data collected at PLB25 contained so much noise that is was not included in the data set for the inversion modelling process (Figure 9).

Noise from the Beverley plant and mine had a negligible effect on data quality, with stations located in close proximity to the mine and plant showing no increased levels of noise. The amount of noise generated by vehicle traffic was minimal, as the area is remote and there were very few vehicles on the road during the survey.

Dimensionality analysis was used to identify potential sources of 3D distortion. The skew and ellipticity of the phase tensors were plotted for each station to determine which frequencies contained 3D effects and required masking. Any phase tensor ellipse where the skew is not is not equal to zero, contains some 2D or 3D effects. Likewise, if the phase tensor is not circular. Phase tensors with skew and ellipticity not equal to zero are known to contain 3D effects. The skew threshold was set to 3° and an ellipticity threshold of 0.1 was used respectively to define 2D and 3D data in agreement with recommendations by Caldwell et al. (2004) and Bibby et al. (2005) respectively. 3D effects were observed at shallow depths at the western end of the survey line, with skew and ellipticity both exceeding their respective threshold values. The 3D effects were initially found, at PL01, in period the range of 0.03 - 0.2 s, gently deepening towards the east. At PL12 the 3D effects were occurring at periods of 2 - 20 s and remain at constant depth for the remain-

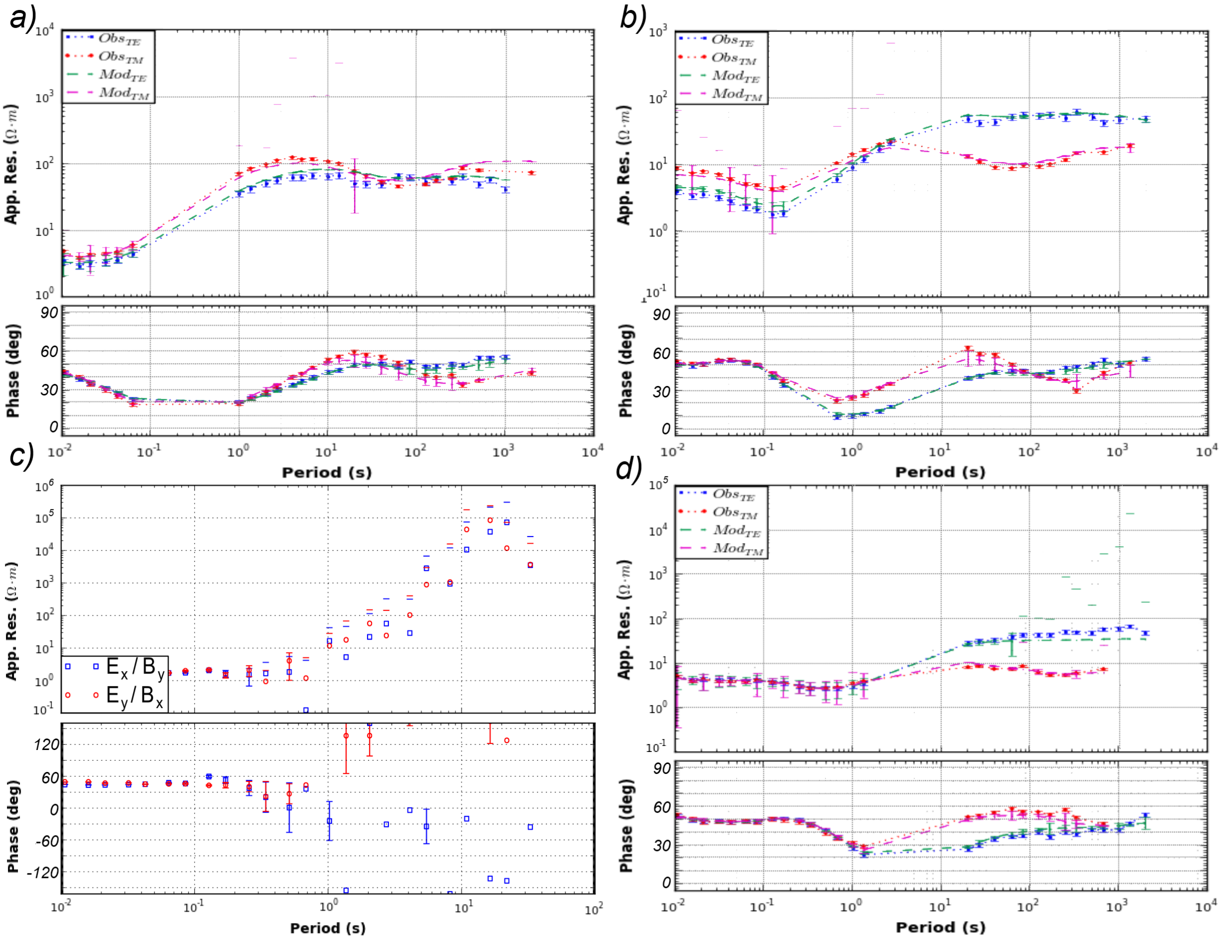

Figure 9: The apparent resistivity and phase plots of the data gathered along the northern line of the Paralana Survey. (a,b,d) Stations PL07, PL10 and PL31 plotted against the Occam model response. The blue circles and red squares represent the TE and TM modes respectively, while the green and purple dashed lines represent the TE and TM model responses. (a) PL07 demonstrates the response from the western end of the survey line, at the base of the Flinders Ranges, near Beverly uranium mine. (b) PL10 is located 3 km east of PL07, the response demonstrates a 2D effects perpendicular to the survey line. This is shown by the split in the TE and TM modes, with the TM mode recording a dip at periods larger than 3 s. (c) PL25 was located in close proximity to the Epic Pipeline, resulting in noisy data of poor quality. This station was removed during processing and was not included in the models. (d) PL31 is located towards the eastern end of the survey line, close to the Paralana borehole. 2D effects are present in the TE mode as at PL10. In comparison to PL10, the high frequency response contains significantly less 2D effects, while the high resistivity response is encountered at longer period (10 s compared with 1 s).

der of the profile (Figure 10). All the data points suffering from 3D effects were masked for 2D inversion modelling. The remaining data from stations at the western end of the profile was found to be very 2D. Skew of between $0 - 3°$ and ellipticity values greater than 0.1 were observed for all data points at periods greater than 0.2 s. The sediments were largely 1D, as expected, with ellipticity less than 0.1 and skew of $0 \pm 1°$ (Figure 10).

Apparent resistivity and phase plots were also used to check data quality. Points that did not fit to the overall smooth curve required by the data were masked due to noise or 3D effects. Splits between the transverse electric (TE) and transverse magnetic (TM) modes on the apparent resistivity plots represent 2D effects in the data (Figure 9). These 2D effects can be attributed to faulting in the region, such as the Wooltana fault, and are preceded by splits in the TE and TM modes of the phase plot. The data gathered on the plains contains splits between the TE and TM modes at longer periods, indicating that the 2D effects are from a deeper source.

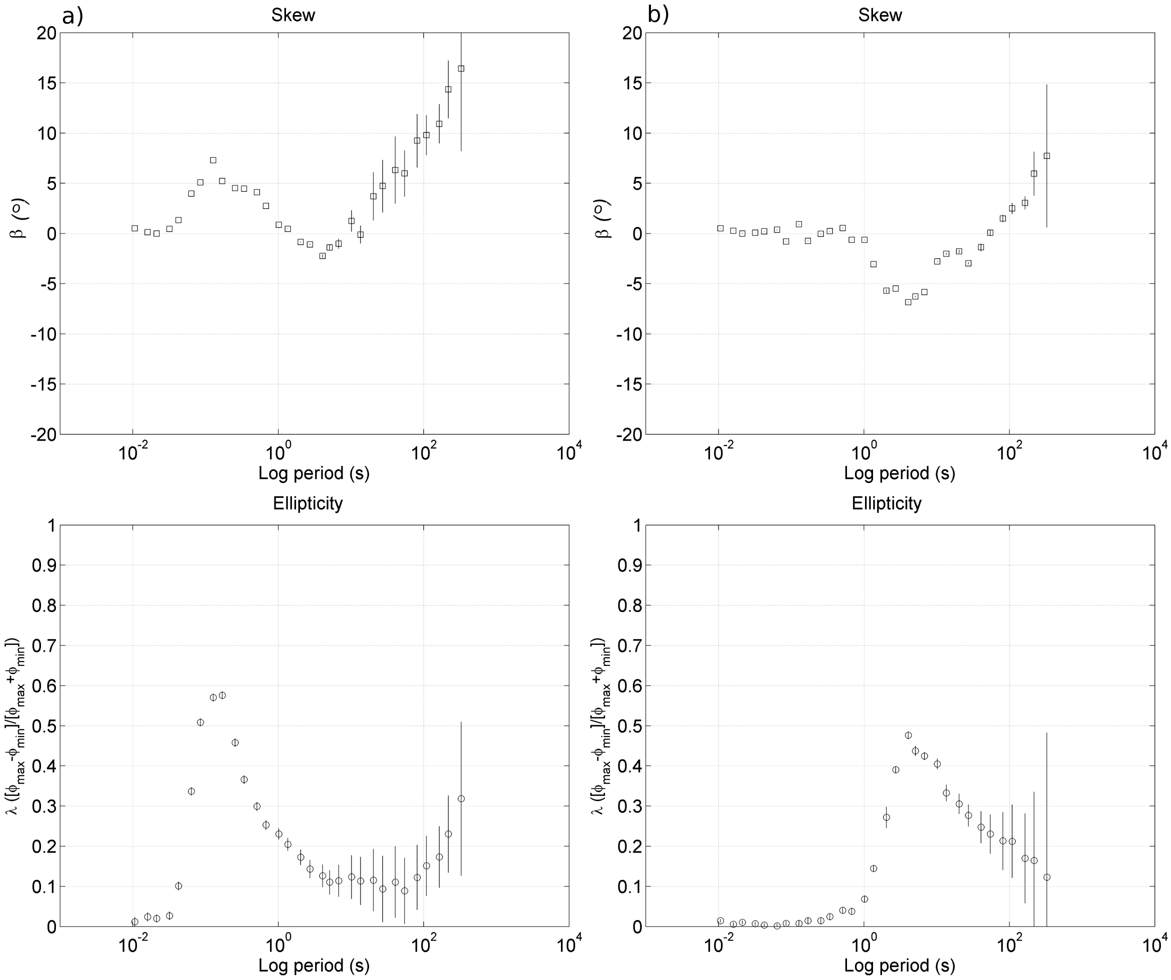

Figure 10: The Skew and Ellipticity plots for stations PL03 and PL28, gathered along the northern survey line. (a) The plots from station PL03 at the western end of the survey, at the base of the Flinders Ranges. The high skew angle at periods around 0.1 s is mirrored by a peak in the ellipticity at the same period. This is indicative of 3D effects in the data and is repeated at long periods. (b) The plots from station PL28, located on the sedimentary plains at the eastern end of the transect, around the Paralana borehole. The peak in the ellipticity coincides with the trough in the skew plot, where the skew angles are less than -3°, this occurs at periods around 3 s. The 3D effected data is at a much greater depth under the plains than close to the ranges.

MODELLING

2D MT Inversion

The northern survey line was modelled in 2D using Occam's inversion algorithm (Figure 3, 11), which finds smooth resistivity models that have the closest fit to the observed data (deGroot Hedlin & Constable 1990; Siripunvaraporn 2012). Smoothing the resistivity model leads to increased uncertainty with depth (deGroot Hedlin & Constable 1990). The model contains both the TE and TM modes of the broadband and long-period data over the period range of 0.01 s to 2000 s. Resistivity and phase error bars were set to 10% and 5% respectively and the data was rotated 2.9° east to geoelectric strike. An initial resistivity of 100 Ω m was used uniformly across the model as the base resistivity. The resulting model had a final root mean square (rms) of 2.22 and a smoothness of 290. The rms is a statistical measure of the data fit to the model, where an ideal fit is 1, anything below 1 is a over fit of the data and a value above 1 contains misfit.

A 50 Ω m conductivity anomaly was detected under the Paralana borehole, with limbs extending to the surface at Paralana and Beverley. A large 20 Ω m conductive body was observed at approximately 20 to 30 km depth, with a thickness of 10 km. A strong resistive body in the order of 10000 Ω m is present at the western end of the model. It extends from the surface to 15 km depth, dipping towards the east. The highly conductive sediment layer is seen to be thickening from west to east, away from the Flinders Ranges.

Sensitivity analysis was carried out on the 2D inversion model by changing the initial base resistivity for the whole model, with values ranging from 10 to 10000 Ω m. The output models were compared to determine how robust the modelled features were and whether the models contain any artefacts. The resulting models were consistent indicating that the initial model was robust and contained no significant artefacts.

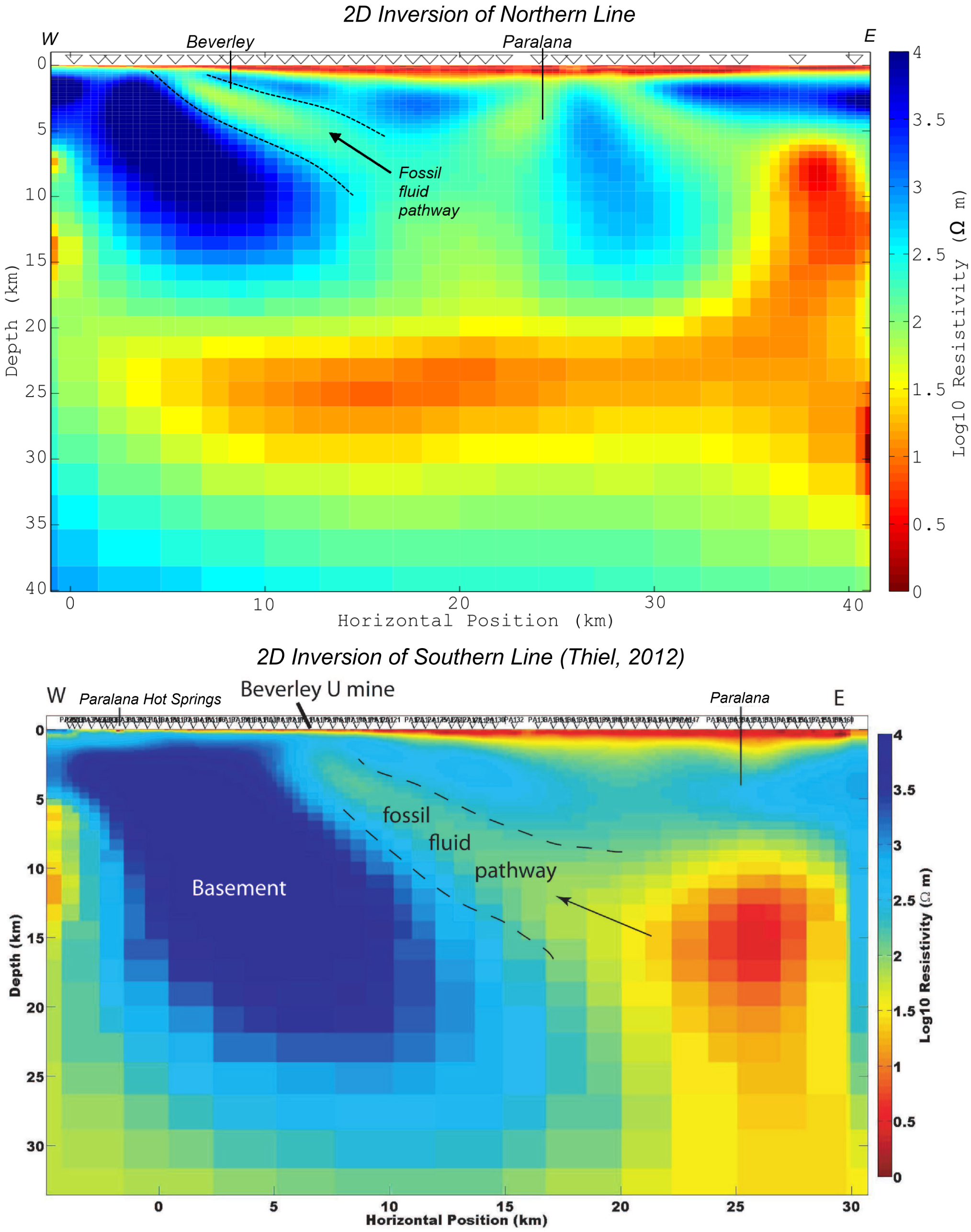

Figure 11: A comparison between the results of 2D inversion modelling of the northern and southern survey lines. The 2D model of the stations along the northern survey line using both the TE and TM modes of broadband and long-period data. The data has a period range of 0.01 s to 2000 s and has been rotated to geoelectric strike before modelling, achieving a RMS of 2.22 and a roughness of 290. High conductivity is shown in red, while the highly resistive structures are represented in blue. A conductive body was observed at 20 km depth, with conductive pathways protruding towards the surface at several locations, including Paralana and at Beverley. The 2D inversion of the southern line was done by Thiel et al. (2012) and contains both the TE and TM modes. The southern line starts further to the west and contains a projection of the Paralana Hot Springs. The features shown in both models are comparable but show geological evolution between survey lines.

3D MT Inversion

Due to available computing power and limitations of 3D modelling algorithm, two separate 3D models were produced (Figure 12). The 3D inversion Occam algorithm only allows 60 station locations and 12 frequencies per station in each model due to limitations in the program and the amount of computing power required to run the inversion (Siripunvaraporn et al. 2005; Siripunvaraporn & Egbert 2009). These limitations significantly reduce the resolution of the models, resulting in broad scale models without small scale definition (Figure 12). Dense grid modelling of smaller areas provided greater resolution over a smaller area. A broad scale model of the entire survey region and a dense grid model centred around the Paralana borehole were produced (Figure 3).

The broad scale model contained 59 stations spread over the whole survey area, with each site containing data across 12 frequencies from 0.004 to 64 Hz. The model was first run with parameters ($\tau = 5$, $x = 0.3$, $y = 0.3$, $z = 0.3$) to generate an initial smooth model. The smoothing parameter is defined by τ and the data fit is controlled by the North (x), East(y) and vertical (z) components where higher values results in a smoother model with less data fit. After 3 iterations the model was stopped and used as the starting conditions for a rough model with better data fit. The rough model had smoothing parameters (5, 0.1, 0.1, 0.1) and data was made to fit within 5% error bars on the off diagonal, and 50% error bars on the diagonal components. The final resulting model had an rms of 1.91.

The dense grid model was centralised around the Paralana borehole and consisted of 60 stations with data across 12 frequencies from 0.006 to 63 Hz. The model was run using the same process as the broad scale model and with the same smoothing parameters and error bars, resulting in a final model with a rms of 1.38.

The 3D inversion models provide comparative results to the 2D model. A large, highly resistive body exists under the Flinders Ranges and extends east under the entire survey. The highly conductive sediments thicken towards the east, away from the ranges in the same way as in the 2D model. The 3D model of the entire survey area only contains broad scale features, with the small features observed in the 2D models, such as the conductive pathway to Beverley, not present. The 3D model demonstrates the evolution of the resistive structure, with the resistive structure being more extensive on the northern side than on the southern side. The dense grid modelled around the Paralana borehole provides evidence that the resistive basement rock contains pathways of high conductivity from depth to the surface (Figure 12).

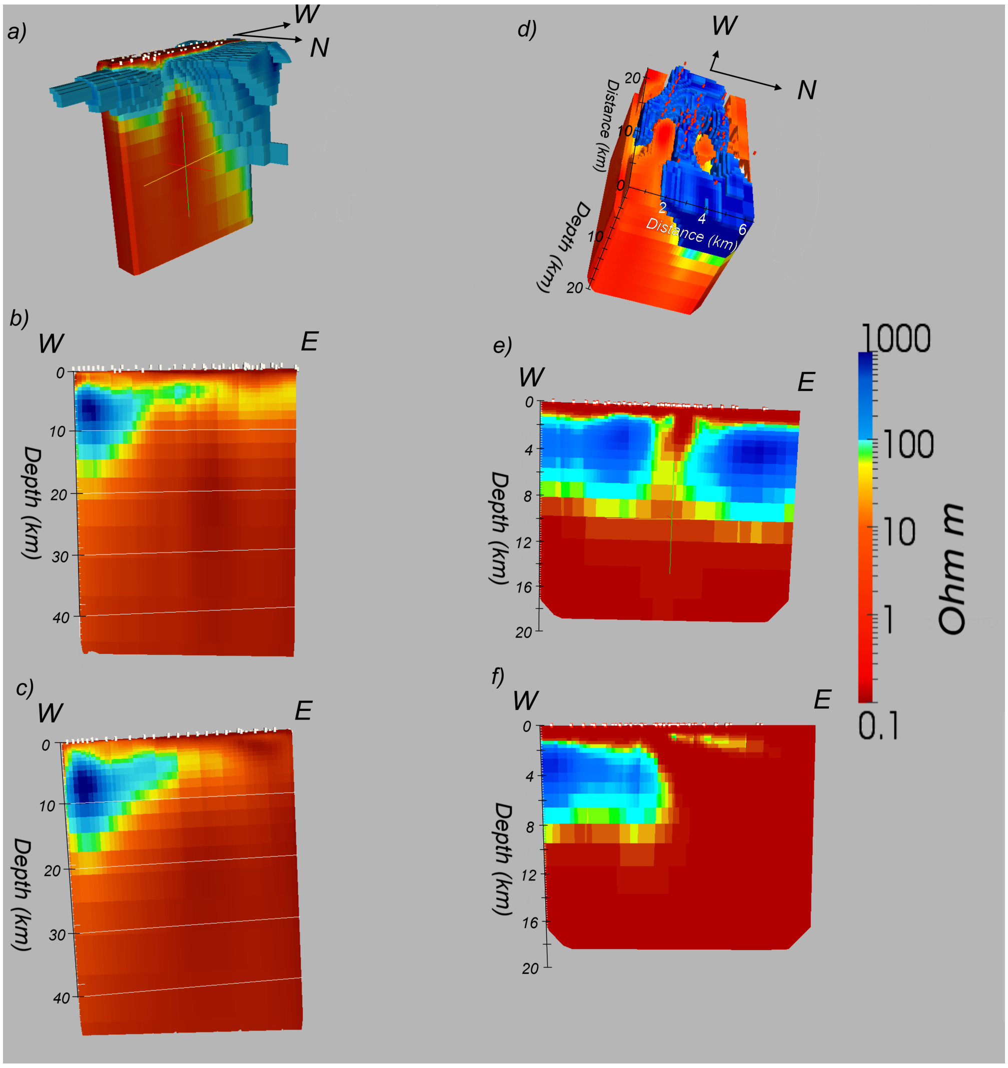

Figure 12: Results of 3D Occam inversion modelling of the north and south lines. a) A broad scale model of the north and south lines, encompassing Beverley Uranium Mine and the Paralana EGS with station locations marked in white. The Resistive basement is observed to be thick in the west and thinning towards the east, with sediments thickening on top. b) A 2D cross section of the broad scale 3D model (a), taken along the line of the northern survey. The resistive basement is clearly visible on the western side of the section, extending as a thinner, slightly more conductive feature towards the east. c) A 2D cross section of the broad scale 3D model (a), taken along the southern survey line. The resistive basement is presented as a more consolidated feature in the west when compared to the northern line. d) A dense grid model centred around the Paralana borehole with station locations marked in red. The model extends to half the depth of the broad scale model (a) with smaller features present. Conductive pathways extending to the surface are visible as holes in the resistive basement. e) A cross section taken along the northern survey line to encompass the dense grid model (d). A conductive pathways is observed linking the surface to a conductor at 10 km depth. f) A 2D cross section through the dense grid model (d) along the southern survey line. The conductive pathway observed at the northern line is no longer present, but has been replaced by the extension of the deep conductor through to the surface.

DISCUSSION

2D MT Inversion

The 2D inversion model was compared with the previous model of the South line by Thiel et al. (2012) to determine similarities. One feature that is consistent across both the North and South lines, is the large conductive anomaly located at 20 to 30 km depth. Deep conductive anomalies have been subject to much conjecture all over the world, with several possible explanations put forward. Aqueous fluids have been a source commonly cited for crustal conductivity (Ohloeft 1981; Shankland 1989; Hyndman & Shearer 1989; Jödicke 1992; Glover 1996; Glover & Ádám 2008; Yang 2011). Although fluids can be used to explain conductive anomalies in the upper crust, the lower crust is dominated by anhydrous granulite facies rock consisting mainly of clinopyroxene, orthopyroxene and plagioclase (Yardley & Valley 1997; Glover & Ádám 2008; Yang 2011). The fact the conductive anomaly seen at Paralana is at the boundary between upper and lower crust makes this an implausible solution to the anomaly's origin.

Partial melt has been put forward as another possible source of high conductivity in the lower crust (Hermance 1979; Glover & Ádám 2008; Yang 2011). For this to be the case, the geothermal gradient must be high enough for partial melt to occur, the crust must be thin and recent tectonic activity must have occurred (Glover & Ádám 2008; Philpotts & Ague 2009; Yang 2011). The geothermal gradient is 50 - 70°C km^{-1} (Cull & Conley 1983) around the MPD and Paralana. Although the geothermal gradient leads to temperatures high enough for partial melt to occur, the region has not undergone any recent tectonism and has a lithospheric thickness in the order of 200 km, leading to the discount of partial melt as the cause of high conductivity (Fishwick et al. 2008; Kennett & Blewett 2012).

Graphite has been proposed as a possible source of high conductivity (Duba & Shankland 1982; Jödicke 1992; Glover 1996; Nover et al. 2005; Jödicke et al. 2007; Glover & Ádám 2008; Yang 2011). Formation of highly conductive graphite films has been found to occur in the presence of CO/CO_2 fluid during fracturing (Roberts et al. 1999; Glover & Ádám 2008). Laboratory results by Nover et al. (2005) have shown graphite crystals can form at temperature and pressure conditions simulating continental crustal conditions. Formations of graphite lead to an increase in the conductivity of the host rock of up to three orders of magnitude (Nover et al. 2005; Glover & Ádám 2008). These results are consistent with the conductive anomaly under Paralana suggesting that it is a large graphite-rich body formed during the uplift of the MPD during the formation of the Flinders Ranges.

The conductive graphite body at 20 to 30 km depth extends towards the surface under the Paralana geothermal prospect, with limbs of high conductivity extending towards the surface at several locations (Figure 11). These conductive limbs are associated with major faults in the region such as the Wooltana Fault and the Paralana Fault. The conductive limb rising under Beverley is likely to be the Poontana Fault, an off shoot of the Wooltana Fault, which Beverley lies adjacent to (Heathgate Resources 1998; Märten 2006). The phase tensor ellipses in Figure 7 provide evidence for this fault. They show a distinct change in ellipticity and orientation in close proximity to Beverley. The higher conductivity observed along the fault (Figure 11) is likely the extension of the graphite body from depth. The presence of graphite along the fault path is consistent the presence of CO/CO_2 fluids traversing the fault during formation. Graphite in the Poontana fault is supportive of the deposition of uranium at the Beverley site due to the reductive environment promoted by the graphite (Skirrow et al. 2009; Farquharson & Craven 2009).

The variations between the two models are indicative of the evolution of the Paralana geothermal prospect from North to South. The northern model is consistent with the southern model with respect to the location of the conductive limb surfacing at Beverley and originating under the Paralana borehole. The conductive body located at 6 km depth under Paralana is consistent in shape but not strength. Thiel et al. (2012) show in their model, a body with resistivity values in the order of 10 Ω m, while the northern line provides a resistivity in the order of 50 Ω m (Figure 11). This could be attributed to a decrease in temperature over the geothermal prospect from the southern line to the northern line or a reduction in the amount of CO/CO_2 fluid present during graphite formation. The decrease in temperature would decrease the extent of alteration and the conductive signature (Simpson & Bahr 2005; Garg et al. 2007; Spichak & Manzella 2009; Aizawa et al. 2011; Peacock et al. 2012). The temperature change would have to be significant for the conductivity to be reduced by a factor of 10, which is not plausible over the space of only a few kilometres. A reduction in the amount of graphite as a result of reduced fluid flow is suggested as the probable cause. Fluid flow could have been decreased due to the discontinuation of faults and fractures towards the north, resulting in reduced fluid pathways and slower graphite formation.

3D MT Inversion

The broad scale 3D model was generally consistent with the 2D inversion model. The large resistive structure that dominates the western end of the model is also present in the 2D model and is interpreted as the MPD making up the base of the Flinders Ranges. The highly conductive sediments are observed to be thickening from west to east, as the distance from the ranges increases (Figure 12). The model also depicts the MPD decreasing in thickness towards the east and a large conductive body underlying it. Around the Paralana borehole, the conductive body at depth penetrates through the MPD to the surface. This is best shown in the dense grid 3D model of the region immediately around the Paralana borehole (Figure 12).

The dense grid model provides evidence for conductive pathways protruding through the MPD to the surface around the borehole. The conductive pathway surfacing at the Paralana borehole in the 2D model of the northern line is visible as a hole in the resistive structure (Figure 12).

Comparison with TMI and Gravity

The total magnetic intensity (TMI) shows high correlation with the 2D and 3D inversions as well as the phase tensors, see Figures 7 and 11. The sediment cover at the base of the Flinders Ranges appears as a featureless plane with a low magnetic response. This plane is abruptly cut by the occurrence of the ranges in the west. The sudden appearance of the ranges corresponds to a band of comparatively very low magnetic response, which is consistent with a conductive limb rising under Beverley in the MT models and a fault response in the phase tensors. The high TMI response in the West corresponds to the Flinders Ranges and is consistent with the highly resistive response from the MT inversion models.

Both the Poontana and Wooltana faults are clearly visible in the gravity image (Figure 13) as linear regions of relatively low gravity in an area of much higher gravity. The relative gravity is high in the ranges and generally low across the plains, but a high anomaly exists just west of the Paralana borehole corresponding to a slight high in the TMI image. This high corresponds to the extension of the 20-30 km deep graphite conductor seen in the MT models. Graphite is a highly conductive mineral but is non-magnetic explaining the absence of the feature in the TMI image. Although graphite has a relatively low density, fine grain boundary films would be enough to increase the conductivity response without a significant decreasing the observed gravity (Nover et al. 2005). The highly resistive MPD rock impregnated with graphite films results in a high gravity response with a conductivity response three orders of magnitude higher than the unaffected MPD rock. The remainder of the gravity image is consistent with the information available in the TMI image in the plains and the low TMI response at the base of the ranges relates well with the gravity data. Interestingly, the images do not correlate well in the Flinders Ranges, where the MPD is present at the surface. The regions of very high gravity response have no direct link with the regions of high TMI.

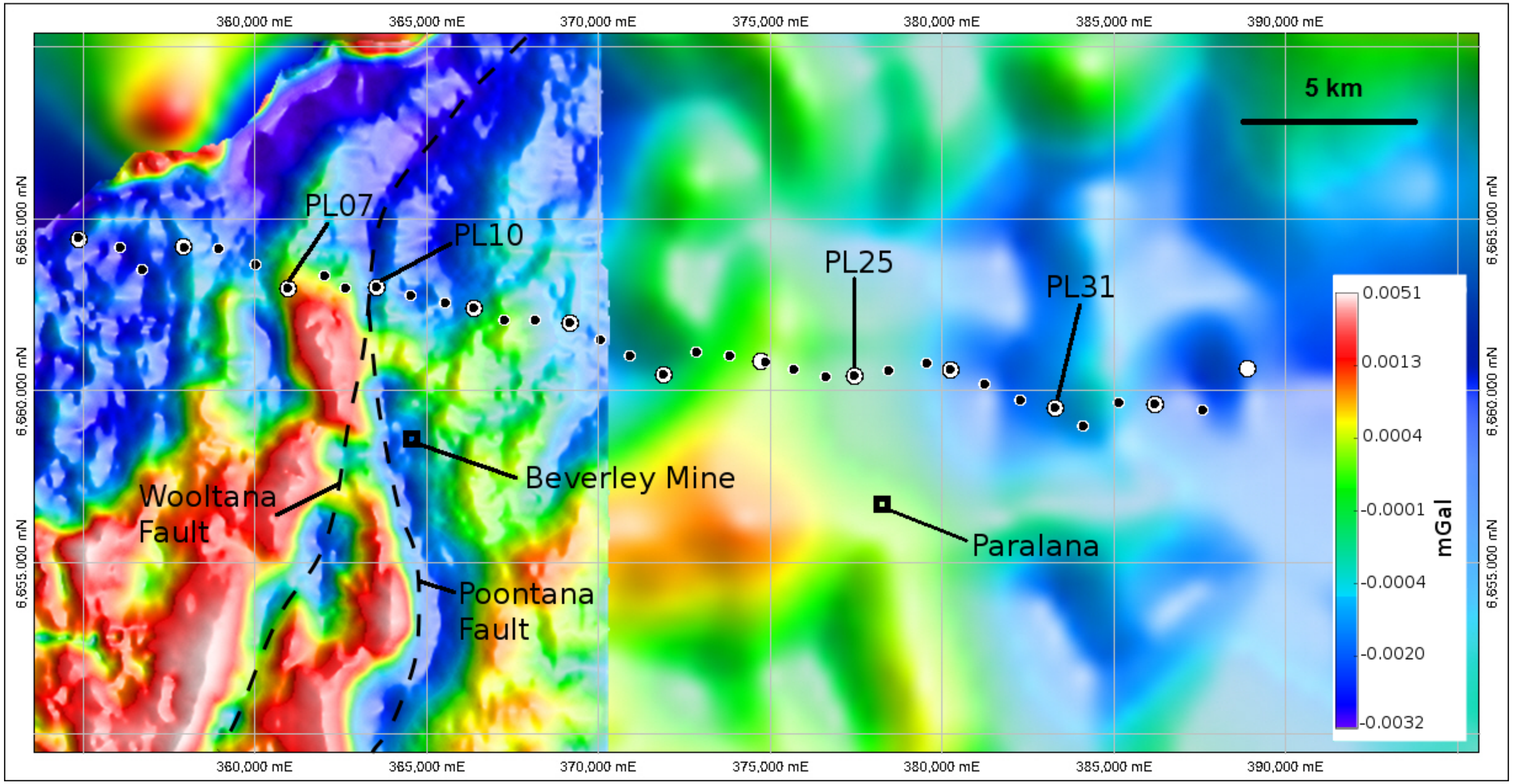

Figure 13: The Bouguer anomaly gravity image of the Paralana area. The Wooltana and Poontana faults are both clearly visible as linear features of low gravity (blue). The Station locations of the northern line are overlayed along with the locations of Beverley and the Paralana borehole. The image is an amalgamation of the separate datasets; the high resolution data in the west was provided by Heathgate Resources, while the rest of the image was collected by PIRSA.

CONCLUSIONS

The high heat flow in the Mt. Painter Domain is caused by the radiogenic decay of the uranium and thorium rich granites in the domain. Uplift and faulting of the Mt. Painter Domain in the Northern Flinders Ranges has resulted in surface expressions of the domain in the ranges. The prospective Paralana EGS is located between the Flinders Ranges and Lake Frome, in the sediments above the Mt. Painter Domain, at a depth of 4 km. MT has been used to delineate a fossil fluid pathway linking deep sourced fluids with the uranium deposit targeted by the Beverley Uranium Mine, 10 km from the range base. This fossil fluid pathway is traced by graphite and is the source of reducing fluids resulting the deposition of the uranium.

ACKNOWLEDGMENTS

I would like to thank Heathgate Resources and Petratherm for their support during this project. In particular, Jonathan Ross, Goran Boren and Philippa Murray for their field work assistance. Lars Krieger for many useful discussions and all his help with fixing programming bugs. Jared Peacock for his processing codes and previous data, without which this project would not be possible. The honours cohort for their support and discussions throughout the year, and finally my project supervisor Stephan Thiel for his teaching, support, and guidance throughout the project.

REFERENCES

Aizawa, K., Kanda, W., Ogawa, Y., Iguchi, M., Yokoo, A., Yakiwara, H. & Sugano, T. (2011). Temporal changes in electrical resistivity at sakurajima volcano from continuous magnetotelluric observations, *Journal of Volcanology and Geothermal Research* **199**(1–2): 165 – 175.

Bibby, H. M., Caldwell, T. G. & Brown, C. (2005). Determinable and non-determinable parameters of galvanic distortion in magnetotellurics, *Geophysical Journal International* **163**(3): 915–930.

Booker, J. (2012). Magnetotelluric phase tensor evolution, *Presented at the 21st Electromagnetic Induction Workshop.*

Brugger, J., Long, N., McPhail, D. & Plimer, I. (2005). An active amagmatic hydrothermal system: The paralana hot springs, northern flinders ranges, south australia, *Chemical Geology* **222**(1-2): 35–64.

Caldwell, T. G., Bibby, H. M. & Brown, C. (2004). The magnetotelluric phase tensor, *Geophysical Journal International* **158**(2): 457–469.

Chave, A. D. & Thomson, D. J. (1989). Some comments on magnetotelluric response function estimation, *J. Geophys. Res.* **94**(B10): 14215–14225.

Chave, A. D. & Thomson, D. J. (2004). Bounded influence magnetotelluric response function estimation, *Geophysical Journal International* **157**(3): 988–1006.

Coats, R. & Blissett, A. (1971). Regional and economic geology of the mount painter province, *Geological Survey of South Australia* **43**: 409–420.

Constable, S. C., parker, R. L. & Constable, C. G. (1987). Occam's inversion: A practical algorithm for generating smooth models from electromagnetic data, *Geophysics* **52**: 289–300.

Cox, R. & Barron, A. (1998). Great artesian basin : resource study, pp. 222–235.

Cull, J. (1982). An appraisal of australian heat-flow data, *Journal of Australian Geology and Geophysics* **7**: 11–21.

Cull, J. & Conley, D. (1983). Geothermal gradients and heat flow in australian sedimentary basins., *BMR Journal of Australian Geology and Geophysics* **8**: 329–337.

deGroot Hedlin, C. & Constable, S. (1990). Occam's inversion to generate smooth, two-dimensional models from magnetotelluric data, *Geophysics* **55**(12): 1613–1624.

Duba, A. & Shankland, T. (1982). Free carbon and electrical conductivity in the mantle., *Geophysical Research letters* **11**: 1271–1274.

Farquharson, C. & Craven, J. (2009). Three-dimensional inverson of magnetotelluric data for mineral exploration: An example from the mcarthur river uranium deposit, saskatchewan, canada, *Journal of Applied Geophysics* pp. 450–458.

Fishwick, S., Heintz, M., Kennett, B. L. N., Reading, A. M. & Yoshizawa, K. (2008). Steps in lithospheric thickness within eastern australia, evidence from surface wave tomography, *Tectonics* **27**: TC4009–.

Fridleifsson, I., Bertani, R., Huenges, E., Lund, J., Ragnarsson, A. & Rybach, L. (2008). The possible role and contribution of geothermal energy to the migigation of climate change, *IPCC Scoping Meeting on Renewable Energy Sources* pp. 59–80.

Garg, S. K., Pritchett, J. W., Wannamaker, P. E. & Combs, J. (2007). Characterization of geothermal reservoirs with electrical surveys: Beowawe geothermal field, *Geothermics* **36**(6): 487–517.

Glover, P. W. J. (1996). Graphite and electrical conductivity in the lower continental crust, *Phys. Chem. Earth* **21**: 279–287.

Glover, P. W. J. & Ádám, A. (2008). Correlation between crustal high conductivity zones and seismic activity and the role of carbon during shear deformation, *J. Geophys. Res.* **113**: B12210–.

Heathgate Resources (1998). Beverley uranium mine: Environmental impact statement.

Heise, W., Caldwell, T. G., Bibby, H. M. & Bannister, S. C. (2008). Three-dimensional modelling of magnetotelluric data from the Rotokawa geothermal field, Taupo Volcanic Zone, New Zealand, *Geophysical Journal International* **173**(2): 740–750.

Hermance, J. F. (1979). The electrical conductivity of meaterials containing partial melt, *Geophys. Res. Lett.* **6**: 613–616.

Huenges, E. & Ledru, P. (eds) (2010). *Geothermal Energy Systems: Exploration, Development and Utilization*, WILEY-VCH verlag GmbH.

Hyndman, R. D. & Shearer, P. M. (1989). Water in the lower continental crust: Modeling magnetotelluric and seismic reflection results, *Geop* **98**: 343–365.

Jödicke, H. (1992). Water and graphite in the earth's crust - an appraoch to interpretation of conductivity models, *Surveys in Geophysics* **13**: 381–407.

Jödicke, H., Nover, G., Kruhl, J. H. & Markfort, R. (2007). Electrical properties of a graphite-rich quartzite from a former lower continental crust exposed in the serre san bruno, calabria (southern italy), *Physics of the Earth and Planetary Interiors* **165**(1–2): 56 – 67.

Kennett, B. L. N. & Blewett, R. S. (2012). Lithospheric framework of australia, *Episodes* **35**: 9–22.

Ketcham, R. (1996). Distribution of heat-producing elements in the upper and middle crust of southern and west central arizona: Evidence from the core complexes, *Journal of geophysical research* **101**: 13611–13632.

Märten, H. (2006). Environmental management and optimization of in-situ-leaching at beverley, *in* B. J. Merkel & A. Hasche-Berger (eds), *Uranium in the Environment*, Springer Berlin Heidelberg, pp. 537–546. 10.1007/3-540-28367-6_54.

McLennan, S. & Taylor, S. (1996). Heat flow and the chemical composition of continental crust., *Journal of Geology* **104**: 369–379.

Neumann, N., Sandiford, M. & Foden, J. (2000). Regional geochemistry and continental heat flow: implications for the origin of the south australian heat flow anomaly, *Earth and Planetary Science Letters* **183**: 107–120.

Newman, G. A., Gasperikova, E., Hoversten, G. M. & Wannamaker, P. E. (2008). Three-dimensional magnetotelluric characterization of the coso geothermal field, *Geothermics* **37**(4): 369–399.

Nover, G., Stoll, J. B. & Von Der Gönna, J. (2005). Promotion of graphite formation by tectonic stress - a laboratory experiment, *Geophysical Journal International* **160**(3): 1059–1067.

Ohloeft, G. R. (1981). Electrical properties of granite with implications for the lower crust, *J. Geophys. Res.* **86**: 931–936.

Peacock, J. R., Thiel, S., Reid, P. & Heinson, G. (2012). Magnetotelluric monitoring of a fluid injection: Example from an enahnced geothermal system, *Geophysical Research Letters* **39**: L18403.

Petratherm (2012). Paralana.

Philpotts, A. R. & Ague, J. (2009). *Principles of Igneous and Metamorphic Petrology (2nd ed.)*, Cambridge university Press.

Pinet, C. & Jaupart, J. (1987). The vertical distribution of radiogenic heat production in the precambrian crust of norway and sweden: Geothermal implication, *Geophys. Res. Lett.* **14**: 260–263.

PIRSA (2011). Curnamona province.

Preiss, W. (1990). A stratigraphic and tectonic overview of the adelaide geosyncline, south australia, *South Australia Department of Mines and Energy* .

Preiss, W. & Forbes, B. (1981). Stratigraphy, correlation and sedimentary history of adelaidean (late proterozoic) basins in australia, *Precambrian Research* **15**: 255 – 304.

Roberts, J. J., Duba, A., Mathez, E. A., Shankland, T. & Kinsler, R. (1999). Carbon-enhanced electrical conductivity during fracture of rocks, *J. Geophys. Res.* **104**: 737–747.

Rudnick, R. L., McDonough, W. F. & O'Connell, R. J. (1998). Thermal structure, thickness and composition of continental lithosphere, *Chemical Geology* **145**: 395–411.

Sandiford, M., Hand, M. & McLaren, S. (1998). High geothermal gradient metamorphism during thermal subsidence, *Earth and Planetary Science Letters* **163**: 149–165.

Shankland, T. J. (1989). A case of two conductors, *Nature* **340**: 102.

Simpson, F. & Bahr, K. (2005). *Practical Magnetotellurics*, Cambridge.

Siripunvaraporn, W. (2012). Three-dimensional magnetotelluric inversion: An introductory guide for developers and users, *Surveys in Geophysics* **33**: 5–27. 10.1007/s10712-011-9122-6.

Siripunvaraporn, W. & Egbert, G. (2009). Wsinv3dmt: Vertical magnetic field transfer function inversion and parallel implementation, *Physics of the Earth and Planetary Interiors* **173**(3–4): 317 – 329.

Siripunvaraporn, W., Egbert, G., Lenbury, Y. & Uyeshima, M. (2005). Three-dimensional magnetotelluric inversion: data-space method, *Physics of the Earth and Planetary Interiors* **150**: 3 – 14.

Skirrow, R., Jaireth, S., Huston, D., Bastrakov, E., Schofield, A., van der Wielen, S. & Barnicoat, A. (2009). Uranium mineral systems: Processes, exploration criteria and a new deposit framework, *Geoscience Australia* **20**: 1–57.

Spichak, V. & Manzella, A. (2009). Electromagnetic sounding of geothermal zones, *Journal of Applied Geophysics* **68**(4): 459–478.

Thiel, S., Peacock, J., Soeffky, P. & Heinson, G. (2012). Fault-controlled uranium emplacement imaged using magnetotellurics, Poster at 21st Electromagnetic Induction Workshop, Darwin, Australia.

Tuncer, V. (2007). *Exploration for unconformity type uranium deposits with audio-magnetotelluric data: A case study from the McArthur river mine, Saskatchewan, Canada*, PhD thesis, University of Alberta.

Yang, X. (2011). Origin of high electrical conductivity in the lower continental crust: A review, *Surveys in Geophysics* **32**: 875–903.

Yardley, B. W. D. & Valley, J. W. (1997). The petrological case for a dry lower crust, *J. Geophys. Res.* **102**: 12173–12185.

APPENDIX A: ADDITIONAL INFORMATION – PART I

Table 1: Data processing table, showing processing parameters for each station.

station	days	latitude	longitude	start	stop	rrstation	rrstart	rrstop	thetae	decimation factor	recorded frequency
PLB01	120	-30.14	139.493	7	17	PLremote	7	17	0,90,180	1	500
PLB02	120	-30.15	139.506	9	19	PLremote	9	19	0,90,180	1	500
PLB03	120	-30.15	139.512	9	19	PLremote	9	19	0,90,180	1	500
PLB04	120	-30.15	139.525	9	19	PLremote	9	19	0,90,180	1	500
PLB05	120	-30.15	139.535	9	19	PLremote	9	19	0,90,180	1	500
PLB06	128	-30.15	139.546	7	17	PLremote	7	17	180, 270, 180	1	500
PLB07	124	-30.16	139.556	9	19	PLremote	9	19	0,270,180	1	500
PLB08	121	-30.15	139.567	7	17	PLremote	7	17	0,90,180	1	500
PLB09	121	-30.16	139.573	10	20	PLremote	10	20	0,90,180	1	500
PLB10	124	-30.16	139.583	9	19	PLremote	9	19	180,90,180	1	500
PLB11	122	-30.16	139.593	7	17	PLremote	7	17	0,90,180	1	500
PLB12	122	-30.16	139.604	7	17	PLremote	7	17	0,90,180	1	500
PLB13	125	-30.16	139.612	7	17	PLremote	7	17	180, 270, 180	1	500
PLB14	122	-30.17	139.621	7	17	PLremote	7	17	0,90,180	1	500
PLB15	122	-30.17	139.631	7	17	PLremote	7	17	0,90,180	1	500
PLB16	124	-30.17	139.641	9	19	PLremote	9	19	180, 270, 180	1	500
PLB17	123	-30.17	139.65	12	22	PLB17	12	22	0,90,180	1	500
PLB18	124	-30.18	139.722	8	18	PLremote	8	18	0,90,180	1	500
PLB19	126	-30.18	139.669	9	19	PLremote	9	19	0,90,180	1	500
PLB20	123	-30.17	139.679	7	17	PLremote	7	17	0,90,180	1	500
PLB21	125	-30.18	139.689	7	17	PLremote	7	17	180, 270, 180	1	500
PLB22	128	-30.18	139.7	7	17	PLremote	7	17	0,90,180	1	500
PLB23	125	-30.18	139.709	7	17	PLremote	7	17	0,90,180	1	500
PLB24	125	-30.18	139.718	7	17	PLremote	7	17	0,90,180	1	500
PLB25	128	-30.18	139.727	7	17	PLremote	7	17	180, 270, 180	1	500
PLB26	128	-30.18	139.738	7	17	PLremote	7	17	180, 270, 180	1	500
PLB27	128	-30.18	139.749	7	17	PLremote	7	17	180,90,180	1	500
PLB28	127	-30.18	139.756	9	19	PLremote	9	19	0,90,180	1	500
PLB29	128	-30.18	139.766	7	17	PLremote	7	17	0,90,180	1	500
PLB30	127	-30.19	139.777	9	19	PLremote	9	19	0,90,180	1	500
PLB31	127	-30.19	139.787	9	19	PLremote	9	19	0,90,180	1	500
PLB32	127	-30.20	139.796	9	19	PLremote	9	19	180, 270, 180	1	500
PLB33	126	-30.19	139.807	7	17	PLremote	7	17	0,270,180	1	500
PLB34	126	-30.19	139.818	7	17	PLremote	7	17	0,270,180	1	500
PLB35	126	-30.19	139.832	7	17	PLremote	7	17	0,270,180	1	500
PLL01	126, 127, 128	-30.14	139.493	9,0,0	24,24,21	ASP	9,0,0	24,24,21	0,270,180	10	1
PLL04	126, 127, 128	-30.14	139.524	5,0,0	24,24,19	ASP	5,0,0	24,24,19	0,90,180	10	1
PLL07	121, 122, 123	-30.16	139.556	23,0,0	24,24,2	ASP	23,0,0	24,24,2	0,270,180	10	1
PLL10	121, 122, 123	-30.16	139.583	9,0,0	24,24,10	ASP	9,0,0	24,24,10	0,90,180	10	1
PLL13	121, 122, 123	-30.16	139.612	9,0,0	24,24,14	ASP	9,0,0	24,24,14	0,270,180	10	1
PLL16	122, 123	-30.17	139.641	9,0	24,16	ASP	9,0	24,16	180, 270, 180	10	1
PLL19	123, 124, 125	-30.18	139.669	23,0,0	24,24,9	ASP	23,0,0	24,24,9	180, 270, 180	10	1
PLL22	123, 124, 125	-30.18	139.699	9,0,0	24,24,10	ASP	9,0,0	24,24,10	0,270,180	10	1
PLL25	124, 125, 126, 127	-30.18	139.727	9,0,0,0	24,24,24,24	ASP	9,0,0,0	24,24,24,24	0,270,180	10	1
PLL28	127, 128, 129	-30.18	139.756	9,0,0	24,24,15	ASP	9,0,0	24,24,15	0,90,180	10	1
PLL31	127, 128	-30.19	139.787	5,0	24,22	ASP	5,0	24,22	0,90,180	10	1
PLL34	127, 128	-30.19	139.818	3,0	24,22	ASP	3,0	24,22	0,270,180	10	1
PLL37	125, 126	-30.18	139.846	4,0	24,10	ASP	4,0	24,10	0,90,180	10	1
PLL41	124, 125, 126	-30.19	139.938	9,0,0	24,24,15	ASP	9,0,0	24,24,15	180, 270, 180	10	1
PLL44	124, 125, 126	-30.19	139.906	9,0,0	24,24,14	ASP	9,0,0	24,24,14	180, 270, 180	10	1

Table 2: Station information table, showing recording information at each station location.

station	date	elevation	ex	ey	magori	magtype	coil	dlbox	harddrive	intbox	battery	start volt	end volt	cacherate	box no	notes
PLB01	29/04/2012	175	47.5	47.7	bx,by	bb	247, 248	5937	5944	17	17	12.37	12.44	001000	17	na
PLB02	29/04/2012	148	48.6	46.2	bx,by	bb	129, 131	5941	5969	20	18	11.11	12.2	001000	20	na
PLB03	29/04/2012	140	40.5	46.5	bx,by	bb	112, 114	5940	5447	11	38	12.37	12.45	001000	11	na
PLB04	29/04/2012	136	50	43.5	bx,by	bb	263, 268	5934	5443	26	1	12.31	12.45	001000	18	na
PLB05	29/04/2012	126	43	50	bx,by	bb	127, 128	5938	5454	23	23	11.92	12.56	001000	23	na
PLB06	7/05/2012	119	46.5	46.4	bx,by	bb	269, 266	5434	5944	21	40	13.51	13.04	001000	21	Ex at 180
PLB07	3/05/2012	120	47.7	47.8	bx,by	bb	263, 268	5441	5944	8	12	12.89	12.05	001000	8	Ey at 270
PLB08	30/04/2012	119	46.3	48.6	bx,by	bb	250, 251	5434	5446	21	39	12.6	12.58	001000	21	na
PLB09	30/04/2012	109	47.3	48.8	bx,by	bb	269, 268	5936	5953	19	45	12.54	12.41	001000	19	na
PLB10	3/05/2012	86	46.7	49.5	bx,by	bb	127, 128	5430	5446	24	29	13.06	12.26	001000	24	na
PLB11	1/05/2012	80	45.8	45.3	bx,by	bb	263, 268	5941	5453	20	47	12.8	12.53	001000	20	na
PLB12	1/05/2012	77	48.5	50	bx,by	bb	127, 128	5938	5951	23	55	12.52	12.3	001000	23	na
PLB13	3/05/2012	69	44.2	47.4	bx,by	bb	247, 248	5429	5447	12	45	13.49	12.48	001000	12	Ey at 270
PLB14	1/05/2012	71	45.5	47.8	bx,by	bb	247, 248	5937	5942	17	24	13.16	12.49	001000	17	na
PLB15	1/05/2012	70	45.6	46	bx,by	bb	131, 129	5934	5971	26	16	13.03	12.3	001000	18	na
PLB16	3/05/2012	65	46	47	bx,by	bb	129, 131	5437	5955	9	46	12.5	12.48	001000	9	electrics rotated by 180
PLB17	2/05/2012	62	44.1	49	bx,by	bb	112, 114	5936	5972	19	18	13.27	12.31	001000	19	elecrics rotated by 180
PLB18	2/05/2012	59	44.8	45.4	bx,by	bb	250, 251	5434	5943	21	1	13.34	12.37	001000	21	electrics rotated by 180, windy
PLB19	5/05/2012	55	47	48	bx,by	bb	131, 129	5939	5971	22	18	12.55	12.41	001000	22	elecrics rotated by 180
PLB20	2/05/2012	56	47	50	bx,by	bb	266, 269	5940	5977	11	38	13.34	12.3	001000	11	na
PLB21	4/05/2012	50	47	45.3	bx,by	bb	114, 112	5936	5956	19	40	13.43	12.52	001000	19	Ey at 270
PLB22	7/05/2012	44	46.7	44.7	bx,by	bb	131, 129	5939	5959	22	33	13.4	12.69	001000	22	na
PLB23	4/05/2012	47	48	50	bx,by	bb	269, 268	5940	5942	11	24	12.78	12.49	001000	11	na
PLB24	4/05/2012	46	48	49	bx,by	bb	251, 250	5434	5453	21	47	12.98	12.66	001000	21	na
PLB25	7/05/2012	44	46	45	bx,by	bb	251, 250	5934	5942	26	8	13.51	12.73	001000	18	Ey at 270
PLB26	7/05/2012	42	44.9	45.4	bx,by	bb	112, 114	5936	5455	20	24	13.48	12.61	001000	19	Ey at 270
PLB27	7/05/2012	44	48	45.5	bx,by	bb	247, 248	5429	5955	12	23	12.73	12.2	001000	12	Ex at 180, had stopped recording
PLB28	7/05/2012	39	46	46.4	bx,by	bb	128, 127	5937	5952	17	16	12.88	12.2	001000	17	on same sheet as PLL28
PLB29	7/05/2012	34	49.5	50	bx,by	bb	269, 266	5430	5444	24	47	12.95	12.2	001000	24	na
PLB30	6/05/2012	32	48.4	47.2	bx,by	bb	269, 268	5936	5454	19	2	13.28	12.77	001000	19	na
PLB31	6/05/2012	30	43.5	48.2	bx,by	bb	114, 112	5940	5446	11	17	13.27	12.78	001000	11	na
PLB32	6/05/2012	27	47	48.5	bx,by	bb	251, 250	5434	5447	21	29	13.4	12.9	001000	21	Ey at 270
PLB33	5/05/2012	28	48	46.3	bx,by	bb	267, 268	5430	5977	24	1	12.15	12.43	001000	24	Ey at 270
PLB34	5/05/2012	28	48	47	bx,by	bb	127, 128	5441	5455	8	16	12.66	12.52	001000	8	Ey at 270
PLB35	5/05/2012	27	45	50	bx,by	bb	247, 246	5429	5976	12	38	12.87	12.42	001000	12	Ey at 270
PLL01	5/05/2012	174	47.3	42.2	bx,by	lp	1120	5433	5969	7	55	13.4	12.59	010000	7	na
PLL04	5/05/2012	132	47	46	bx,by	lp	1126	5437	5951	9	7	12.81	12.51	010000	9	na
PLL07	30/04/2012	120	47.7	47.8	bx,by	lp	1119	5441	5976	8	40	12.49	12.53	001000	8	na
PLL10	30/04/2012	86	46.7	49.5	bx,by	lp	1116	5430	5959	24	7	12.52	12.3	001000	24	na
PLL13	30/04/2012	69	44.2	47.4	bx,by	lp	1184	5429	5455	12	33	12.09	12.4	001000	12	na
PLL16	1/05/2012	65	46	47	bx,by	lp	1118	5437	5956	9	8	12.73	12.43	001000	9	Electrics rotated by 180
PLL19	2/05/2012	55	47	48	bx,by	lp	1126	5939	5952	22	17	12.6	12.49	010000	22	na
PLL22	2/05/2012	53	47.6	49.7	bx,by	lp	1120	5433	5451	7	2	13.24	12.45	010000	7	na
PLL25	3/05/2012	44	46	45	bx,by	lp	1118	5934	5443	26	39	13.39	12.4	010000	18	Ey at 270
PLL28	7/05/2012	39	46	46.4	bx,by	lp	1119	5941	5451	19	12	12.88	12.2	010000	20	on same sheet as PLB28
PLL31	6/05/2012	33	43.5	44.2	bx,by	lp	1116	5938	5943	23	45	12.85	12.76	010000	23	na
PLL34	6/05/2012	28	48	47	bx,by	lp	1184	5441	5972	8	46	12.89	12.64	010000	8	Ey at 270
PLL37	4/05/2012	23	45.8	44.6	bx,by	lp	1119	5941	5959	20	33	13.36	12.55	010000	20	na
PLL41	3/05/2012	17	42.4	44	bx,by	lp	1184	5937	5444	17	23	12.66	12.23	010000	17	electrics rotated by 180
PLL44	3/05/2012	17	45	44.7	bx,by	lp	1116	5938	5953	23	8	12.7	12.16	010000	23	electrics rotated by 180
PLremote	29/04/2012	109	1	1	bx,by	bb	133, 132	5447	5448	25	2	13.61	12.55	001000	25	solar panel
ASP	29/04/2012	1	1	1	bx,by,bz	lp	1	1	1	1	1	12.95	12.3559	000001	1	observatory
CNB	29/04/2012	1	1	1	bx,by,bz	lp	1	1	1	1	1	12.9621	12.3462	000001	1	observatory